

1 **Impact of grids and dynamical cores in CESM2.2 on**
2 **the surface mass balance of the Greenland Ice Sheet**

3 **Adam R. Herrington¹, Peter H. Lauritzen¹, Marcus Lofverstrom², Andrew**
4 **Gettelman¹**

5 ¹National Center for Atmospheric Research, 1850 Table Mesa Drive, Boulder, Colorado, USA

6 ²Department of Geosciences, University of Arizona, 1040 E. 4th Street, Tucson, AZ USA

7 **Key Points:**

- 8
- 9 • The transition from latitude-longitude to unstructured grids in CESM negatively
impacts the surface mass balance of the Greenland Ice Sheet.
 - 10 • Two new Arctic refined mesh configurations have been developed and made avail-
able in CESM2.2
 - 11 • The Arctic meshes provide improvements to the surface mass balance over all 1°
grids, including latitude-longitude grids.
- 12
- 13

14 **Abstract**

15 Six different configurations, a mixture of grids and atmospheric dynamical cores
 16 available in the Community Earth System Model, version 2.2 (CESM2.2), are evaluated
 17 for their skill in representing the climate of the Arctic and the surface mass balance of
 18 the Greenland Ice Sheet (GrIS). The more conventional 1° – 2° uniform resolution grids
 19 systematically overestimate both the accumulation and ablation processes over the GrIS.
 20 Of these conventional grids, the latitude-longitude grids outperform the quasi-uniform
 21 unstructured grids owing to their greater degrees of freedom in representing the GrIS.
 22 Two Arctic refined-meshes, containing $\frac{1}{4}^{\circ}$ and $\frac{1}{8}^{\circ}$ refinement over Greenland, are doc-
 23 umented in this study as newly supported configurations in CESM2.2. The Arctic meshes
 24 provide substantial improvements to the simulated cloud field in the Arctic and over Green-
 25 land, resulting in a skillful representation of the accumulation and ablation processes,
 26 and a more realistic GrIS surface mass balance compared with the conventional, uniform
 27 resolution grids. As CESM is in the process of transitioning away from latitude-longitude
 28 grids, these new Arctic refined meshes serve to recover, and improve upon the represen-
 29 tation of polar processes in CESM.

30 **Plain Language Summary**

31 [enter your Plain Language Summary here or delete this section]

32 **1 Introduction**

33 General Circulation Models (GCMs) are powerful tools for understanding the me-
 34 teorology and climate of the high-latitudes, which are among the most sensitive regions
 35 on Earth to global and environmental change. Despite their importance, the numerical
 36 treatment of polar regions in GCMs is handled in vastly-different ways due to the so-
 37 called *pole-problem* (D. Williamson, 2007). The pole problem refers to numerical insta-
 38 bility arising from the convergence of meridian lines into polar singularities on latitude-
 39 longitude grids (e.g., Figure 1a). Depending on the numerics, methods exist to suppress
 40 this instability, and latitude-longitude grids may be advantageous for polar processes as
 41 structures can be represented with more degrees of freedom than elsewhere in the com-
 42 putational domain. With the recent trend towards globally uniform unstructured grids,
 43 any potential benefits of latitude-longitude grids on polar regions may become a relic of
 44 the past. In this study a number of grids and dynamical cores (hereafter referred to as
 45 *dycores*) available in the Community Earth System Model, version 2.2 (CESM2.2; Dan-
 46 abasoglu et al., 2020), including brand new variable-resolution grids, are evaluated to
 47 understand their impacts on the simulated characteristics of the Arctic, with a special
 48 focus on the climate and surface mass balance of the Greenland Ice Sheet.

49 In the 1970's the pole problem was largely defeated through wide-spread adoption
 50 of efficient spectral transform methods in GCMs. These methods transform grid point
 51 fields into a global, isotropic representation in wave space, where linear operators (e.g.
 52 horizontal derivatives) in the equation set can be solved for exactly. While spectral trans-
 53 form methods are still used in the 21st century, local numerical methods have become
 54 desirable for their ability to run efficiently on massively parallel systems. The pole prob-
 55 lem has thus re-emerged in contemporary climate models that use latitude-longitude grids,
 56 and some combination of reduced grids and polar filters are necessary to ameliorate this
 57 instability (Jablonowski & Williamson, 2011). Polar filters are akin to a band-aid; they
 58 subdue the growth of unstable modes by applying additional damping to the solution
 59 over polar regions. This additional damping reduces the effective resolution in polar re-
 60 gions such that the resolved scales are approximately the same everywhere on the grid.

An alternative approach is to use unstructured grids, which allow for more flexible grid structures that permit quasi-uniform grid spacing globally and eliminates the pole-problem entirely (e.g., Figure 1c). This grid flexibility also permits variable-resolution or regional grid refinement (e.g., Figure 2). Grids can be developed with refinement over polar regions that could in principle make up for any loss in polar resolution in transitioning away from latitude-longitude grids (e.g., Figure 2), although this comes at the cost of a smaller CFL-limiting time-step in the refined region (the CFL-condition — short for Courant–Friedrichs–Lowy condition — is a necessary condition for numerical stability when using discrete data in time and space). Unstructured grids also scale more efficiently on parallel systems than latitude-longitude grids, likely resulting in a greater prevalence of unstructured grids as computing power continued to increase over time.

The meteorology and climate of the Arctic is characterized by a range of processes and scales that are difficult to represent in GCMs (Bromwich et al., 2001; Smirnova & Golubkin, 2017; van Kampenhout et al., 2018). For example, while synoptic scale storms are generally well represented at typical GCM resolutions of 1 to 2 degrees (Jablonowski & Williamson, 2006; Stocker, 2014), mesoscale Polar Lows are not well resolved at these resolutions. These mesoscale systems are prevalent during the cold season and produce gale-force winds that can induce large heat and moisture fluxes through the underlying sea-ice/ocean interface. The Arctic also contains the Greenland Ice Sheet (hereafter denoted as *GrIS*). While it blankets the largest island in the world (Greenland), many of the processes that control the GrIS annual surface mass balance (the integrated sum of precipitation and runoff) are only partially resolved at typical GCM resolutions. For example, GrIS precipitation is concentrated at the ice-sheet margins, where orographic precipitation is generated by steep topographic slopes. GrIS ablation areas (marginal regions where seasonal melting exceeds the annual mass input from precipitation) are typically 10s to 100 km wide and confined to low-level areas or regions with limited precipitation. GCMs struggle to resolve the magnitude and extent of these features (Pollard, 2010; van Kampenhout et al., 2018), which can lead to unrealistic ice sheet growth in models with an interactive ice sheet component (e.g., Lofverstrom et al., 2020).

The goal of this study is to characterize the representation of high-latitude regions using the spectral-element and finite-volume dycores in CESM2.2, as these models treat the high-latitudes, e.g., the pole-problem, in different ways. The manuscript is laid out as follows: Section 2 consists of documentation of the grids, dycores and physical parameterizations used in this study. The Arctic refined grids were developed by the authors, and this section serves as their official documentation in CESM2.2. Section 2 also contains a description of the experiments along with the datasets and methods for evaluating the model simulations. Section 3 contains the results of the experiments, followed by Section 4 that provides a general discussion and conclusions.

2 Methods

2.1 Dynamical cores

The atmospheric component of CESM2.2, the Community Atmosphere Model, version 6.3 (CAM; Craig et al., 2021), supports a number of different atmospheric dynamical cores. These include dycores using latitude-longitude grids, such as finite-volume (FV; Lin, 2004) and eulerian spectral transform (EUL; Collins et al., 2006) models, and dycores built on unstructured grids, including spectral-element (SE; Lauritzen et al., 2018) and finite-volume 3 (FV3; Putman & Lin, 2007) models. The EUL dycore is the oldest dycore in CAM, and the least supported of all the dycores. FV3 is the newest dycore in CAM, but it was not fully incorporated at the time this work commenced; both the EUL and FV3 dycores are omitted from this study. As such, the results presented in this study are comparing the performance of the SE and FV dycores.

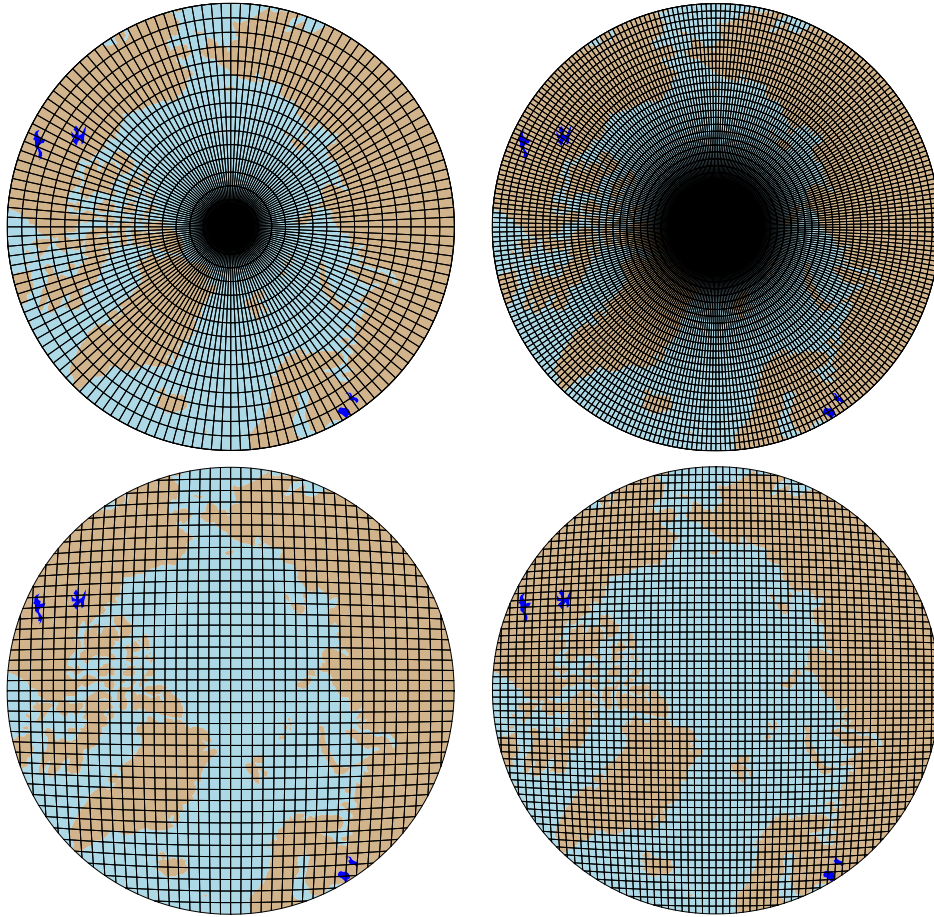


Figure 1. Computational grids for the uniform $1^\circ - 2^\circ$ grids in this study.

2.1.1 Finite-volume (FV) dynamical core

The FV dycore is a hydrostatic model that integrates the equations of motion using a finite-volume discretization on a spherical latitude-longitude grid (Lin & Rood, 1997). The 2D dynamics evolve in floating Lagrangian layers that are periodically mapped to Eulerian reference grid in the vertical (Lin, 2004), using a hybrid-pressure vertical coordinate. Hyperviscous damping is applied to the divergent modes while Laplacian damping is applied to momentum in the top few layers, referred to as a *sponge layer* (Lauritzen et al., 2011). A polar filter is used to avoid computational instability due to the convergence of the meridians, allowing for a more practical time-step. It takes the form of a Fourier filter in the zonal direction, with the damping coefficients increasing monotonically in the poleward direction (Suarez & Takacs, 1995).

2.1.2 Spectral-element (SE) dynamical core

The SE dycore is a hydrostatic model that integrates the equations of motion using a high-order continuous Galerkin method (Taylor et al., 1997; Taylor & Fournier, 2010). The computational domain is a cubed-sphere grid tiled with quadrilateral elements (e.g., Figure 2). Each element contains a fourth order basis set in each horizontal direction, with the solution defined at the roots of the basis functions, the Gauss-Lobatto-Legendre (GLL) quadrature points. This results in 16 GLL nodal points within each element, with 12 of the points lying on the (shared) element boundary. Communication between el-



Figure 2. Spectral-element grid for the variable-resolution ARCTIC grid in this study. Note that this is not the computational grid; each element has 3×3 independent grid points.

ements happens via the direct stiffness summation (Canuto et al., 2007), which applies a numerical flux to the element boundaries that reconciles overlapping nodal values and produces a continuous global basis set.

As with the FV dycore, the dynamics evolve in floating Lagrangian layers that are subsequently mapped to an Eulerian reference grid. A dry mass vertical coordinate was more recently implemented for thermodynamic consistency with condensates (Lauritzen et al., 2018). The 2D dynamics have no implicit dissipation and so hyperviscosity operators are applied to all prognostic variables to remove spurious numerical errors (Dennis et al., 2012). Laplacian damping is applied in the sponge layer.

The SE dycore supports regional grid refinement via its variable-resolution configuration, requiring two enhancements over uniform resolution grids. (1) As the numerical viscosity increases with resolution, explicit hyperviscosity relaxes according to the local element size, reducing in strength by an order of magnitude per halving of the grid spacing. A tensor-hyperviscosity formulation is used (Guba et al., 2014), which adjusts the coefficients in two orthogonal directions to more accurately target highly distorted quadrilateral elements. (2) The topography boundary conditions need to be smoothed in a way that does not excite grid scale modes, and so the NCAR topography software (Lauritzen et al., 2015) has been modified to scale the smoothing radius by the local element size.

For spectral-element grids with quasi-uniform grid spacing, a variant in which tracer advection is computed using the Conservative Semi-Lagrangian Multi-tracer transport scheme (CSLAM) is used instead (Lauritzen et al., 2017). CSLAM has improved tracer property preservation and accelerated multi-tracer transport. It uses a separate grid from the spectral-element dynamics, through dividing each element into 3×3 control volumes with quasi-equal area. The physical parameterizations are computed from the state on the CSLAM grid, which has clear advantages over the default SE dycore in which the physics are evaluated at the GLL nodal points (A. Herrington et al., 2018).

2.2 Grids

Six grid are evaluated in this study (Table 1). The FV dycore is run with 1° and 2° grid spacing, referred to as $f09$ and $f19$, respectively (Figure 1a,b). The 1° equivalent of the CAM-SE-CSLAM grid is also run, referred to as $ne30pg3$ (Figure 1c), where

grid name	dycore	Δx_{eq} (km)	Δx_{refine} (km)	Δt_{phys} (s)
<i>f19</i>	FV	278	-	1800
<i>f09</i>	FV	139	-	1800
<i>ne30pg2</i>	SE-CSLAM	167	-	1800
<i>ne30pg3</i>	SE-CSLAM	111	-	1800
<i>ne30pg3*</i>	SE-CSLAM	111	-	450
<i>ARCTIC</i>	SE	111	28	450
<i>ARCTICGRIS</i>	SE	111	14	225

Table 1. Grids and dycores used in this study. Δx_{eq} refers to average equatorial grid spacing, Δx_{refine} refers to grid spacing in the refined region (if applicable) and Δt_{phys} refers to the physics time-step. The dycore abbreviation FV refers to the finite-volume dycore, SE the spectral-element dycore and SE-CSLAM the spectral-element dycore w/ CSLAM tracer advection.

ne refers to a grid with $ne \times ne$ elements per cubed-sphere face, and *pg* denotes that there are $pg \times pg$ control volumes per element for computing the physics. An additional 1° CAM-SE-CSLAM grid is run, but with the physical parameterizations computed on a grid that contains 2×2 control volumes per element, *ne30pg2* (Figure 1d; A. R. Herrington et al., 2019).

Two variable resolution meshes were developed as part of the CESM2.2 release that contains grid refinement over the Arctic (Figure 2). This manuscript serves as the official documentation of these grids. The Arctic meshes were developed using the software package SQuadgen (<https://github.com/ClimateGlobalChange/squadgen>). The *ARCTIC* grid is a 1° grid with $\frac{1}{4}^\circ$ regional refinement over the broader Arctic region. The *ARCTICGRIS* grid is identical to the *ARCTIC* grid, but contains an additional patch covering the big island of Greenland with $\frac{1}{8}^\circ$ resolution.

The physics time-step should depend on grid resolution. Increases in horizontal resolution permit faster vertical velocities that reduce characteristic time-scales, and so the physics time-step is reduced to avoid large time truncation errors (A. Herrington & Reed, 2018). The *ARCTIC* and *ARCTICGRIS* grids are run with a $4 \times$ and $8 \times$ reduction in physics time-step relative to the default 1800 s time-step used in the standard $1^\circ - 2^\circ$ grids (Table 1).

All grids and dycores in this study use 32 levels in the vertical, with a model top of about 1 hPa or about 40 km. However, any grid or dycore can in principle be run with a higher-top and/or with finer vertical resolution.

2.3 Physical parameterizations

The CAM6.3 physical parameterization package (hereafter referred to as the *physics*; Craig et al., 2021) is used in all simulations in this study. CAM version 6 physics and later is most notably different from its predecessors through the incorporation of high-order turbulence closure, Cloud Layers Unified by Binormals (CLUBB; Golaz et al., 2002; Bogenschutz et al., 2013), which jointly acts as a PBL, shallow convection and cloud macro-physics scheme. CLUBB is coupled with the MG2 microphysics scheme (Gettelman et al., 2015), with prognostic precipitation and classical nucleation theory in representing cloud ice for improved cloud-aerosol interactions. Deep convection is parameterized using a convective quasi-equilibrium, bulk plume mass flux scheme (Zhang & McFarlane, 1995; Neale et al., 2008) and includes convective momentum transport (Richter et al., 2010). PBL form drag is modeled after (Beljaars et al., 2004) and orographic gravity wave drag is represented with an anisotropic method informed by the orientation of topographic ridges at the sub-grid scale.

Initial simulations with the *ne30pg3* spectral-element grid produced weaker short-wave cloud forcing relative to the tuned up finite-volume dycore. All runs with the spectral-element dycore have two CLUBB parameter changes in order to provide a more realistic cloud forcing and top-of-atmosphere radiation balance. These are CLUBB's *gamma* parameter, reduced from 0.308 to 0.270, and *c14*, reduced from 2.2 to 1.6. Briefly, the *gamma* parameter scales the width of the sub-grid distribution of vertical velocity, and *c14* controls the strength of the damping term in the equation for the horizontal component of turbulent kinetic energy. For a thorough explanation of how CLUBB parameters impact the simulated climate, the reader is referred to (Guo et al., 2015).

2.4 Experimental design

All grids and dycores are run using an identical transient 1979-1998 AMIP-style configuration, with prescribed monthly SST/sea-ice after (Hurrell et al., 2008). This configuration refers to the *FHIST compset* and runs out of the box in CESM2.2.

The surface mass balance (SMB) of the Greenland Ice Sheet (GrIS) is simulated in all grids and dycores in this study. The SMB is the sum of the mass accumulation term, i.e., precipitation, and the mass sink term, ablation. Ablation can be expressed as evaporation/sublimation plus total runoff, with runoff being a combination of liquid precipitation and snow and ice melt. Not all liquid precipitation runs-off the ice sheet; rain can penetrate pore spaces in the snowpack/firn layer and freeze, representing an accumulation of mass. These processes are represented by different components in CESM, but it is the Community Land Model, version 5 (CLM; Lawrence et al., 2019), that aggregates these processes and computes the SMB.

CLM runs on the same grid as the atmosphere, but also uses a downscaling technique to account for sub-grid variability in SMB. In short, the ice sheet patch in a CLM grid cell is subdivided into 10 elevation classes (EC), weighted by their respective area fractions at each EC, which is derived from a high resolution GrIS elevation dataset. The near surface air temperature, humidity and air density are calculated at each EC using an assumed lapse rate and the elevation difference from the grid mean, and the precipitation rates from CAM are repartitioned into solid or liquid based on the temperature of the EC. Ice accumulation is modeled as a capping flux, or snow in excess of a 10 m snow cap, and refreezing of liquid within the snowpack additionally acts as a source of ice. A unique surface energy balance and SMB is computed for each EC. Integrating over all ECs using the area weights provides a more accurate SMB. For a more detailed description of how the SMB is computed in CESM, the reader is referred to Lipscomb et al. (2013); Sellevold et al. (2019); van Kampenhout et al. (2020).

Since the 10 m snowcap needs to be reached in the accumulation zone to simulate the SMB, the snow depths in the variable-resolution grids were spun-up by forcing CLM in standalone mode, cycling over a 20 year *ARCTIC FHIST* run for about 500 years. The uniform resolution grids are all initialized with an SMB from an existing *f09* spun-up initial condition.

2.5 Observational Datasets

Several observational datasets are used in this study to gauge the performance of the simulations. A list of the datasets used in this study are provided in Table 2. Several of these products are near-global gridded datasets commonly used to evaluate GCMs. Surface mass balance datasets were initially gathered from several sources. RACMO2.3 11km and RACMO2.3p2 5.5km are regional model simulations targeting Greenland, forced by ERA40, ERA interim and ERA5 reanalysis products at its domain boundaries. The RACMO simulations have been shown to perform skillfully against observations and is often used as an ideal modeling target (Noël et al., 2015, 2019).

data product	years used in this study	resolution	citation
ERA5	1979-1998	$\frac{1}{4}^\circ$	Copernicus (2019)
CERES-EBAF ED4.1	2003-2020	$\frac{1}{4}^\circ$	Loeb et al. (2018)
CALIPSO-GOCCP	2006-2017	1°	Chepfer et al. (2010)
RACMO2.3	1979-1998	11 km	Noël et al. (2015)
RACMO2.3p2	1979-1998	5.5 km	Noël et al. (2019)

Table 2. Description of observational datasets used in this study.

In-situ SMB (snow pit and ice cores) and radar accumulation datasets (e.g., IceBridge) are conveniently maintained in The Land Ice Verification and Validation toolkit (LIVVkit), version 2.1 (Evans et al., 2019). However, these point-wise measurements are difficult to compare to model output spanning several different grids, and would be more useful if the surface mass balance from the individual EC's were available from the model output, which they are not. A nearest neighbor technique was used to do an initial analysis, and indicated that the model biases are similar to those computed using the RACMO datasets. Owing to the uncertainty of comparing gridded fields to point-wise measurements, and the lack of additional information it adds with regard to model biases, these datasets were omitted from the analysis in this study.

2.6 SMB Analysis

We seek to integrate components of the SMB over a GrIS ice mask and diagnose their contributions to the mass budget of the GrIS. However, the ice masks vary across all the grids, especially in comparison to the RACMO3.2 ice mask which is about 3% smaller than the reference dataset (Figure 3). The area errors in Figure 3 may not seem large, but even order 1–2% percent ice mask area differences can lead to large differences in integrated SMB (Hansen et al., 2022). CLM's dataset creation tools generates the model ice mask by mapping a raw high resolution dataset containing the GrIS boundary conditions, to the target grid using the Earth System Modeling Framework (ESMF; Team et al., 2021) first-order conservative remapping algorithm. The figure suggests the mapping errors are less than 1.5% across just the model grids.

In this study we have taken a common ice mask approach by mapping all model fields to the lowest resolution grids and integrating over their respective low resolution ice masks. A low resolution common ice mask is a conservative decision and is largely because we seek to use first-order remapping algorithms for mapping fields to the common ice mask, which is not reliable in the downscaling direction, i.e., mapping to a higher resolution grid than the source grid. Two remapping algorithms are used; ESMF first-order conservative and TempestRemap (Ullrich & Taylor, 2015) high-order monotone algorithm. Due to the sensitivity of mapping errors to grid coordinates (i.e., unstructured or structured), all quantities are evaluated on both the *f19* and *ne30pg2* grids, the lowest resolution grid for each grid coordinate type. In all, each integrated quantity is evaluated (at most) four times per grid to provide an estimate of uncertainty due to differences in grid coordinates and remapping algorithm.

We consider two different approaches for integrating mapped fields over the common ice mask.

- Map the patch level quantities, or the state over the ice fractional component of the grid cell, to the common grid, and integrate the mapped field over the common ice mask.
- Map the grid cell mean quantities to the common grid, and integrate the mapped field over the common ice sheet.

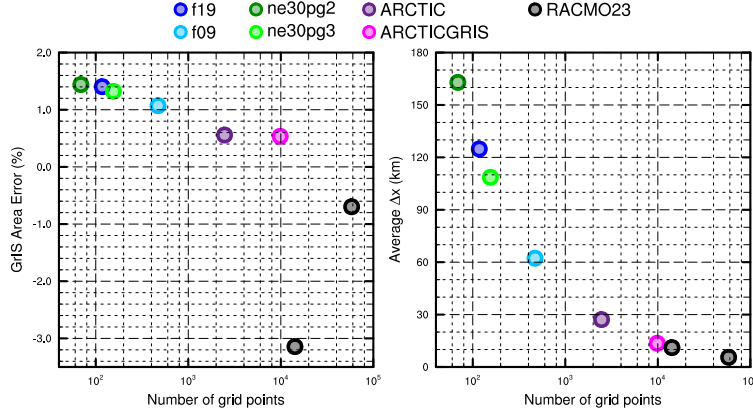


Figure 3. The spatial properties of the GrIS as represented by different grids in this study. (Left) GrIS area error, computed as the relative differences from a 4km dataset used to create the CESM ice masks, (right) approximate average grid spacing over GrIS.

Method 1 introduces errors that is related to differences in the ice mask between the source and target grid. Since the lower resolution ice masks tend to have larger GrIS areas (Figure 3), we expect these errors to inflate the resulting integrals. Method 2 assumes the patch level values are identical to the grid mean values. This has the effect of homogenizing ice mask specific states over the entire grid cell. This is especially detrimental to the ice melt quantity, since ice melt can only occur over the ice mask. The accumulation term (combined solid plus liquid precipitation), however, should not be adversely impacted by method 2 since it is not directly tied to the ice mask, but instead controlled by larger resolved scales. One could also argue that method 1 is less accurate for the accumulation term, since it does not map to the new ice mask as cleanly as in method 2.

Method 2 may be necessary in situations where only the grid mean values are available, and the patch level values cannot be reconstructed. This is unfortunately the case for the RACMO datasets; ice melt cannot be reconstructed at the ice patch level. Method 2 is therefore used in this study, and we should expect a dissipative effect when diagnosing the melt rates. As we will show later, this method still preserves the relative differences between the different grids and in comparison with the RACMO datasets.

3 Results

3.1 Tropospheric temperatures

Before delving into the simulated characteristics of the Arctic, the global mean differences between the various grids and dycores are assessed. Figure 4 shows 1979-1998 annual mean, zonal mean height plots expressed as differences between the uniform resolution grids and dycores. The *f09* grid is warmer than the *f19* grid, primarily in the mid-to-high latitudes and throughout the depth of the troposphere. This is a common response to increasing horizontal resolution in GCMs (Pope & Stratton, 2002; Roeckner et al., 2006), and A. R. Herrington and Reed (2020) has shown that this occurs in CAM due to greater resolved vertical velocities that in turn, facilitate greater condensational heating in the macrophyiscs routine in CLUBB. The right columns in Figure 4 supports this interpretation, which shows an increase in the climatological CLUBB heating in the low and mid-latitudes in the *f09* grid.

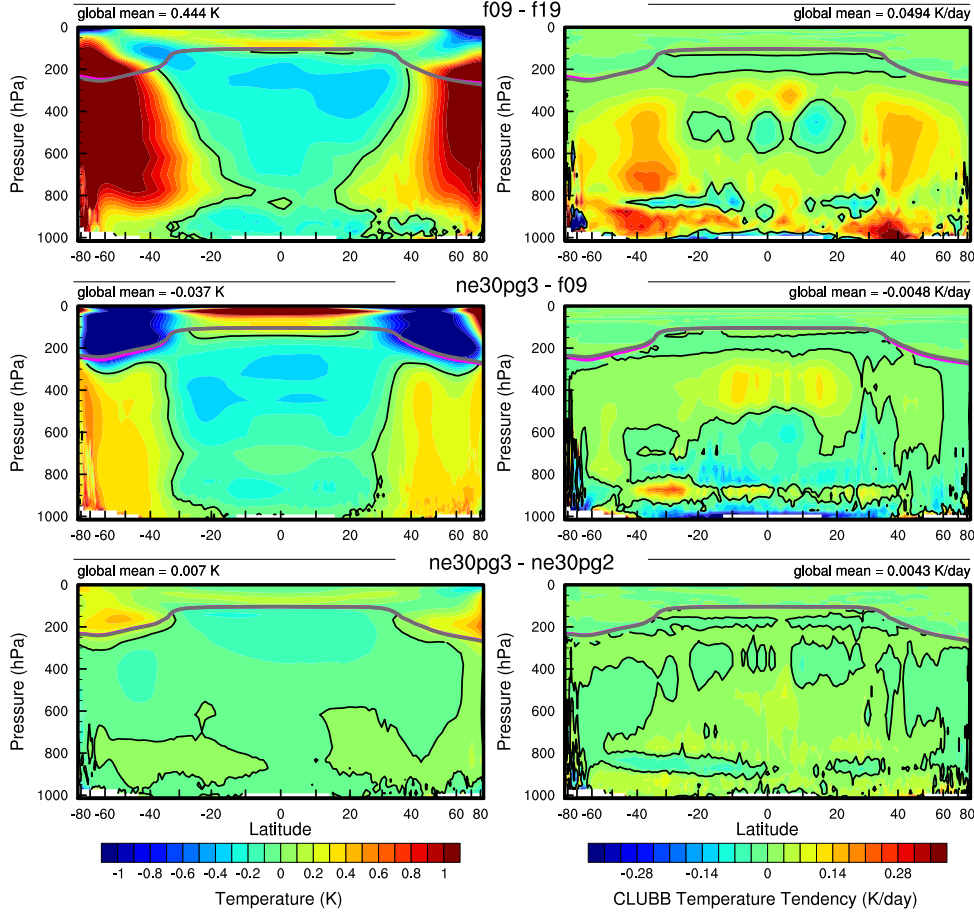


Figure 4. 1979–1998 annual mean (left column) temperature and (right column) CLUBB temperature tendencies in zonal mean height space, expressed as differences between the various $1^\circ - 1^\circ$ grids. The thick grey and magenta lines are the tropopause for control run and the test run, respectively.

As the SE dycore is less diffusive than the FV dycore, the resolved vertical velocities are larger in the SE dycore, and so a modest, resolution-like sensitivity occurs in which *ne30pg3* is warmer than *f09* (Figure 4). The stratosphere has a uniquely different response, in which *ne30pg3* is much cooler than *f09* in the mid-to-high latitudes. Figure 4 also shows differences in temperature between *ne30pg3* and *ne30pg2*, which are small, although there is a slight warming near the tropopause at high latitudes. This is consistent with the similar climates found between these grids in A. R. Herrington et al. (2019).

Comparing the variable-resolution grids to the uniform resolution grids is complicated because we simultaneously increase the grid resolution and reduce the physics time-step, both of which noticeably impact the solution (D. L. Williamson, 2008). An additional *ne30pg3* simulation is run with the physics time-step used in the *ARCTIC* grid, referred to as *ne30pg3**. Figure 5 shows the change in the climatological summer temperatures in zonal-mean height space between *ne30pg3** and *ne30pg3*. A similar warming response to increasing resolution occurs when the time-step is reduced, and the mechanism is similar in that the shorter time-step facilitates greater condensational heating by CLUBB. Figure 5 shows the difference in climatological summer temperature between the *ARCTIC* grid and the *ne30pg3** grid. The greater condensational heating and warmer tempera-

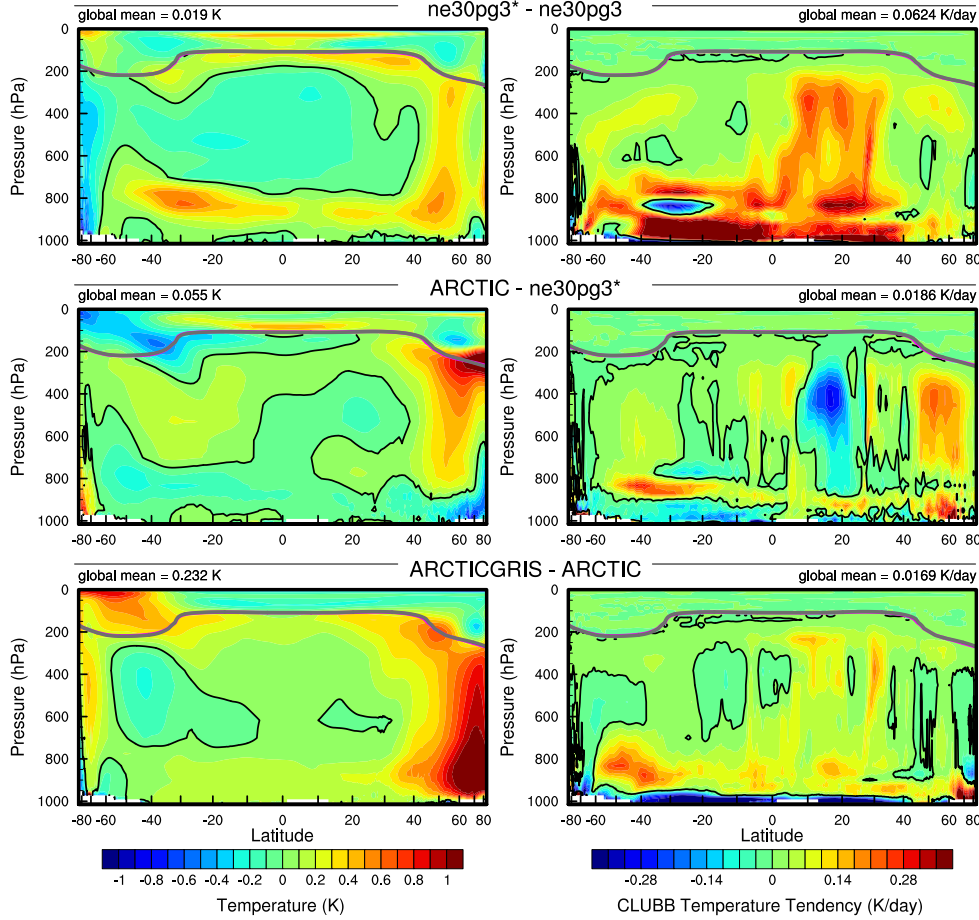


Figure 5. As in Figure 4 but for the short-time step experiment and the variable-resolution grids. The fields plotted are for the climatological northern hemisphere summer. The focus on summer is because that is when the resolution response is largest, and the refined regions are located in the northern hemisphere.

332 tures are confined to the regionally refined region when the impact of physics time-steps
333 is removed from the comparison.

334 Figure 5 indicates that the *ARCTICGRIS* grid is a lot warmer than the *ARCTIC* grid.
335 Part of this may be due to the shorter physics time-step; a similar
336 physics-time-step sensitivity in the *ne30pg3** comparison is evident in the CLUBB ten-
337 dencies in the *ARCTCGRIS* grid. However, the temperature response is disproportio-
338 nately large relative to the change in CLUBB tendencies. This summer warming appears
339 to be a result of variations in the stationary wave pattern, with anomalous southerly winds
340 occurring to the west of Greenland (not shown). This dynamic response is extremely in-
341 teresting because other than the physics time-step, the only difference between *ARCTICGRIS*
342 and the *ARCTIC* grid is the doubling of resolution of Greenland. This behavior will be
343 explored more fully in a future study.

344 It's useful to understand summer temperature biases due to its control on ice/snow
345 melt over the Greenland Ice Sheet (GrIS; Ohmura, 2001). Figure 6 shows the 1979-1998
346 lower troposphere summer temperature bias relative to ERA5. It is computed from the
347 500 hPa-1000 hPa geopotential thickness, solving for the layer mean virtual tempera-

ture using the hypsometric equation. The results generally track with the analysis of the zonal mean height plots; increasing resolution from $f19$ to $f09$ leads to a warmer climate, and the 1° spectral-elements grids are warmer than the finite-volume grids. The summer temperatures in the finite-volume grids are persistently colder than ERA5, whereas the 1° spectral-element grids are not as cold, and are actually warmer than ERA5 at very high-latitudes, north of 75° . All grids illustrate a north-south gradient in bias over Greenland, in which the summer temperature bias becomes more positive on the northern side of the ice sheet. This pattern is also evident in the 2m summer temperature bias over Greenland (not shown).

The *ARCTIC* grid has similar summer temperatures to the 1° spectral-element grids, but it is a bit warmer over northern Eurasia and the North Pole. An anomalous cooling patch forms to the west of Greenland, centered over Baffin Island. The *ARCTICGRIS* grid is warmer than the *ARCTIC* grid over most of the Arctic, but maintains a similar spatail pattern of summer temperature bias as in the *ARCTIC* grid.

Some of these temperature anomalies may be related to summer shortwave cloud forcing differences across the different grids and dycores. Figure 7 shows the summer shortwave cloud forcing bias in the runs, using the CERES-EBAF product. All the uniform 1° – 2° grids have similar biases, with the clouds reflecting 20-40 W/m² too much shortwave radiation over a wide swath of the Arctic, primarily over the land masses. There's also a halo of low cloud forcing bias around the oceanic perimeter of Greenland. The *ARCTIC* grid has much smaller cloud forcing biases over the Arctic land masses, although still too reflective, whereas the *ARCTCGRIS* grid vastly improves the cloud forcing bias over Eurasia, and improves the bias over N.America compared to the *ARCTIC* grid. In both variable-resolution grids, the halo of too weak cloud forcing bias around the perimeter of Greenland is absent.

While the summer cloud forcing biases are consistent with the summer temperature biases in Figure 6 –regions where clouds are too reflective coincide with regions that are too cold– it is not clear whether the cold biases are caused by the cloud biases, or whether the cold biases amplify the cloud forcing bias.

3.2 Shortwave radiation over Greenland

In addition to summer temperatures, shortwave radiation is also an important determinant of snow/ice melt. Figure 8 shows the summer incident shortwave radiation bias at the surface, zoomed in over Greenland. The top panel computes the bias using the CERES-EBAF dataset, and the bottom panel using RACMO2.3p2 dataset. This halo of excessive incident shortwave radiation around the coasts of Greenland is apparent in both datasets, consistent with the shortwave cloud forcing biases in Figure 7.

The interior of the ice sheet receives too little shortwave radiation in the coarser grids. In the variable-resolution grids, both the interior deficit in shortwave and the excessive shortwave around the oceanic perimeter of Greenland are improved. This suggests that the coarse grids clouds are too thick in the interior of Greenland, and too thin around the perimeter of Greenland, and that increasing horizontal resolution balances out these biases. This is consistent with total summer cloud fraction bias, computed from the CALIPSO-GOCCP cloud dataset (Figure 9). Note that total cloud fraction characterizes the cloud field at all vertical levels, but attenuates any changes arising from any single layer due to the maximum overlap assumption used to compute this quantity. Despite the attenuated signal, the total cloud fraction does indicate a reduction in cloud coverage in the interior, and an increase in cloudiness about the oceanic perimeter, in the variable-resolution grids.

The agreement of the cloud biases in and around Greenland from multiple independent datasets indicates this is a robust feature of the coarser grids. The reduction

grid name	accumulation	total melt	runoff	sublimation	SMB
RACMO	768.5 (733.5)	-347.2 (-436.4)	-221.7 (-258.5)	-36.5 (-38.8)	510.3 (436.2)
f19	882.5 (913.5)	-440.3 (-546.5)	-283.7 (-284.3)	-36.6 (-37.5)	562.2 (591.7)
f09	874.8 (882.1)	-418.4 (-482.3)	-255.0 (-212.3)	-38.1 (-37.4)	581.7 (632.4)
ne30pg2	1000. (973.4)	-549.4 (-647.3)	-383.9 (-347.0)	-33.4 (-32.1)	582.7 (594.3)
ne30pg3	934.9 (909.3)	-568.8 (-686.7)	-356.2 (-330.1)	-34.4 (-32.6)	544.3 (546.6)
ARCTIC	795.9 (818.6)	-367.3 (-436.8)	-208.9 (-194.2)	-44.1 (-43.9)	542.9 (580.5)
ARCTICGRIS	708.7 (747.3)	-471.6 (-610.4)	-261.1 (-307.8)	-50.7 (-51.8)	396.9 (387.7)

Table 3. 1979-1998 surface mass balance of the Greenland Ice Sheet in Gt/yr. Values shown are using the common ice mask approach described in the methods section, whereas values in parentheses are from integrating over the native grid and ice mask.

of these cloud biases in the variable-resolution grids suggests they are a result of insufficient horizontal resolution in the coarse grids.

3.3 Greenland surface mass balance

The accuracy of the simulated SMB is expected to be sensitive to grid resolution. Figure 9 shows the average grid spacing over the Greenland Ice Sheet (GrIS) in all six grids in this study. The *ne30pg2* grid has the coarsest representation with an average $\Delta x = 160 \text{ km}$, and the *ARCTICGRIS* grid has the highest resolution with an average $\Delta x = 14.6 \text{ km}$, similar to the grid spacing of the 11 km RACMO2.3 grid. The *ne30pg3* grid has an average $\Delta x = 111.2 \text{ km}$, which is substantially more coarse than the *f09* grid, with an average $\Delta x = 60 \text{ km}$. This is interesting because *ne30pg3* and *f09* have similar average grid spacing over the entire globe, and comparable computational costs, but due to the convergence of meridians the finite-volume model has enhanced resolution over GrIS. The *ARCTIC* grid has an average grid spacing of $\Delta x = 27.8 \text{ km}$, and is about 10 times more expensive than the 1° models (whereas the *ARCTICGRIS* grid is about twice as expensive as the *ARCTIC* grid).

The summer climatological mean precipitation bias over GrIS is shown in Figure 9, expressed as the fractional difference from the RACMO2.3p2 solution. It is evident that the coarse 1°–2° grids have large, positive biases centered over the southern dome. The *ARCTIC* run improves this bias substantially, and the *ARCTICGRIS* run improves this bias further. This suggests the southern dome bias is due to inadequate horizontal resolution, which is consistent with the original GrIS variable-resolution experiments in (van Kampenhout et al., 2018).

Large accumulation rates in GrIS result from synoptic systems arriving from the south. These systems are orographically lifted at the ice sheet margin, especially the steep slopes in southeast Greenland, concentrating large amounts of precipitation about the ice margin. At lower horizontal resolutions the topography is too smooth and anomalous moisture penetrates inland, erroneously dumping precipitation onto the southern dome. The ability of the variable-resolution grids to more accurately simulate the orographic precipitation process in Greenland is consistent with all the cloud results up to this point. As the precipitation centers move from the interior towards the margins, and even out over the ocean with increasing resolution, the cloud decks should, and are, moved accordingly. Figures 7, 8, 9 clearly illustrate a reduction in cloud amount in the interior and an increased cloudiness around the oceanic perimeter of Greenland, in comparing the uniform 1° – 2° runs to the variable-resolution runs.

Table 3 shows the 1979-1998 climatological SMB components in all the grids, and compared with RACMO. Note the values in the table averages over the ensemble of common ice masks and regridding methods described in section 2.6. The RACMO values are

averages over both RACMO datasets (Table 2) using the same common ice mask approach. The SMB is computed from the individual components as:

$$SMB = accumulation + runoff + sublimation \quad (1)$$

and all terms have consistent sign conventions (positive values contribute mass, negative values reduce mass). Note that this glaciological SMB differs from the internally computed SMB in CLM; see van Kampenhout et al. (2020) for an explanation of the differences.

Table 3 also contains (in parentheses) the SMB components derived from evaluating the integrals on each model's native grid and ice mask. Of note is the large reduction in ice/melt rates using the common ice mask approach compared with that computed on the native grid. This illustrates the dissipative impact of the common ice mask approach discussed in section 2.6. The errors are large because it is mixed ice/ice-free grid cells straddling the ice sheet margins that are more prone to errors, which are commonly in the ablation zone and have large melt rates. Contrast this with the differences in integrated precipitation, where the differences between the native approach and common ice mask approach is much less. As discussed in the methods, this is because the combined solid/liquid precipitation rates are not directly tied to the ice mask, whereas ice melt is exclusively tied to the ice mask.

Figure 10 shows time-series of annually integrated precipitation and snow/ice melt over the GrIS in the various different grids and dycores, with both versions of RACMO shown in black. The 1979-1998 climatological mean values, tabulated in Table 3, are also provided as circles on the right side of the panels. The uniform $1^\circ - 2^\circ$ grids all show a distinctive positive bias in precipitation due to this over-prediction of interior precipitation rates. The variable-resolution grids have the smallest precipitation biases, providing a comparable solution to RACMO. The *f19* and *f09* perform similarly, with +110 Gt/yr bias, whereas *ne30pg3* is biased by about +165 Gt/yr and *ne30pg2*, +230 Gt/yr. The results suggest that uniform resolution spectral-element grids have larger biases than the finite-volume grids, consistent with spectral-element grids having a coarser representation of GrIS (Figure 3).

The combined annual snow/ice melt shown in the bottom panel of Figure 10 indicates that the *ARCTIC* grid simulates the most realistic melt rates, with all other grids tending to have larger melt rates than RACMO. The *ARCTICGRIS* grid over predicts melting by about 125 Gt/yr. This is likely due to an anomalously warm lower troposphere during the summer, relative to the *ARCTIC* run (Figure 6). The *f19* and *f09* melting rates are improved over *ARCTICGRIS*, overestimating melt by only 70-90 Gt/yr. The spectral-element grids have the largest positive melt bias, between 200-220 Gt/yr. It is more difficult to attribute these differences to resolution alone, since the finite-volume grids have colder summer temperatures than the uniform resolution spectral-element grids.

To understand the regional behavior of the SMB components, Figure 11 shows the precipitation and combined snow/ice melt integrated over the basins defined by Rignot and Mouginot (2012). The uncertainty due to differences in basin area is larger than for GrIS wide integrals, owing to the differences in basin boundaries as represented by the common ice masks, which can be seen in the *f19* and *ne30pg2* panels of Figure 12. Nonetheless, the regional totals in Figure 11 correctly show the southeast and southwest basins have the largest accumulation totals. All basins exhibit a monotonic reduction of accumulation rates with increasing grid resolution, with some exceptions. The *ARCTCIGRIS* grid simulates less precipitation than RACMO in the central-east and southeast basins, and is closest of all grids to the RACMO precipitation amounts in the large southwest basin.

The basin integrated melt rates in Figure 11 show a dycore dependent-type pattern. The uniform-resolution spectral-element grids have the largest positive bias in melt

485 rates, in all basins. The *ARCTICGRIS* grid is a close second, while the finite-volume
 486 grids have systematically smaller melt-rates. The “second-place” standing of *ARCTICGRIS*
 487 is somewhat unexpected as this grid has the warmest lower troposphere summer tem-
 488 peratures (Figure 6) and incident shortwave radiation (Figure 8), yet it has less melt-
 489 ing than the uniform-resolution spectral element grids.

490 Lower troposphere temperature is not a strict proxy for melting; e.g., it may not
 491 capture microclimate effects as a result of a better representation of the low-elevation
 492 ablation zones. A more accurate proxy for the impact of temperature on melting is pos-
 493 itive degree-days (PDD; Braithwaite, 1984). PDD is a metric that accumulates the near
 494 surface temperature in $^{\circ}\text{C}$ for any day in which the temperature is above freezing. PDD
 495 is non-linear in mean monthly temperature (Reeh, 1991), and we compute it using monthly
 496 mean 2-meter temperature using the method of Calov and Greve (2005), assuming a fixed
 497 monthly mean standard deviation of 3°C , and a degree-day factor of $5 \text{ mm } d^{-1} \text{ } ^{\circ}\text{C}^{-1}$.

498 The basin integrated PDD melt estimate is shown in Figure 11. One interesting
 499 feature is that in the big southeast and southwest basins (and all the other western basins),
 500 the *ne30pg3* grid has larger PDD based melt than the *ARCTCGRIS* grid. The south-
 501 west basin also predicts a rather large PDD based melt in the finite-volume grids, rel-
 502 ative to the *ARCTCIGRIS* grid. The PDD plots indicate that the near surface tem-
 503 peratures expected to contribute to melt is not well approximated by the summer lower
 504 troposphere temperatures in Figure 6.

505 Figure 12 shows the biases in the combined ice/snow melt as map plots. This plot
 506 is quite revealing as it indicates that the largest melt biases occur on the southeast and
 507 northwest coast, where large coarse grid cells overlap with the ocean. One possibility is
 508 that these problematic grid cells are situated at lower elevations than the ice sheet sur-
 509 face exists in nature, leading to too warm of a state and overestimating the melt. Fig-
 510 ure 13 shows the representation of the surface of the ice sheet along two transects in the
 511 different grids, compared to the high resolution dataset used to generate CAM topog-
 512 raphy boundary conditions (Danielson & Gesch, 2011; Lauritzen et al., 2015). The two
 513 transects are shown in Figure 12; the infamous “k-transect” in southwest Greenland and
 514 a transect extending from the central dome down to the highly productive Kangerlus-
 515 suaq glacier on the southeast coast. The 1° – 2° grids are noticeably coarse, with only
 516 a handful of grid cells populating the transect. The *f09* grid is a bit of an exception; the
 517 grid cells become very narrow in the meridional direction at high latitudes and a larger
 518 number of grid cells populate the east-west transect. The variable-resolution grids are
 519 more skillful at reproducing the steep margins of the ice sheet, capturing the parabolic
 520 shape of the GrIS margins.

521 While the transects in Figure 13 only provide two anecdotes, they indicate that the
 522 ice sheet surface is not systematically lower than the true surface in the coarse grids, in
 523 the ablation zones. Rather the smoothing of the raw topography, necessary to prevent
 524 the model from instigating grid-scale modes, flattens the ice sheet, causing the lower-elevation
 525 ablation zones to extend further outside the true ice sheet margin, and are situated higher
 526 than the actual ice surface. The *f19* grid has the smoothest topography since it’s dy-
 527 namics are coarsest (whereas *f09*, *ne30pg2* and *ne30pg3* use identical smoothing), and
 528 has the flattest ice sheet. This suggests that if anything, coarser models will tend to el-
 529 evate the ablation zones and depress melt rates.

530 Figure 13 also labels the ice margin boundary, which nicely illustrates that the ab-
 531 lation zone occurs over very narrow horizontal distances where the ice sheet rapidly plunges
 532 down to sea-level. Due to this abrupt transition, coarse grids will commonly represent
 533 the ablation zone with mixed grid cells containing mixtures of the ice and ice-free regions.
 534 We hypothesize that the reason that the coarser models tend to have large melt biases,
 535 despite the *ARCTCIGRIS* having the warmest troposphere, is because summer melt-
 536 ing is confined to these mixed ice/land/ocean grid cells. CLM deals with land hetero-

537 geneity in a complex and sophisticated manner, but CAM only see a homogenized state
 538 due to volume averaging over the sub-grid mixture. The implication is that the ice-free
 539 land patches in a grid cell may unduly influence the climate over the entire grid cell, caus-
 540 ing a warm bias over the ice patch of a grid cell.

541 Figure 14 shows mean melt bias, relative to both RACMO datasets, conditionally
 542 sampled based on grid cell ice fraction in the GrIS region. Note the common ice mask
 543 approach is used to compute the errors, meaning all fields are mapped to the common
 544 ice masks and the grid cell ice fraction is defined by the common ice masks. The figure
 545 shows that coarser grids generally have two peaks in ice fraction space; a bump in pos-
 546 itive melting errors on the 0-20% range, and another in the fully ice-covered ice cells. Also
 547 shown are the \pm one standard deviation of the biases for each bin. They indicate that
 548 the biases in 0-20% bins are mostly contained in the positive bias region (a fractional
 549 bias greater than 0), whereas the fully-covered ice cells have a wider distribution, with
 550 many grid cells also containing negative melting biases. The excessive melting that oc-
 551 curs in 0-20% ice fraction bins supports our hypothesis that the prevalence of mixed-grid
 552 cells in representing the ablation zone in coarse grids is responsible for their large melt
 553 bias.

554 3.4 Precipitation extremes

555 Synoptic storms are tracked using TempestExtremes (Ullrich et al., 2021). As the
 556 *ARCTIC* grid contains $\frac{1}{4}^{\circ}$ refinement north of about 45° latitude, the storm tracker is
 557 applied to this region for the *ARCTIC* and *ne30pg3* run to identify differences in storm
 558 characteristics due to horizontal resolution. The composite mean precipitation maps are
 559 similar between the two grids, and exhibit the iconic comma structure of synoptic cy-
 560 clones (not shown).

561 Figure 15 is a PDF of the precipitation rates associated with the storms, by month.
 562 The PDFs are constructed by sampling all the precipitation rates within 30° of the storm
 563 center, for each point on the storm track and for all storms. The PDFs are evaluated on
 564 an identical composite grid for all runs, and so storm statistics are not impacted by dif-
 565 ferences in output resolution. The *ARCTIC* run has larger extreme precipitation rates
 566 compared to *ne30pg3* in every month, but the increase is greatest in the summer months,
 567 which coincides with the most extreme events of the year. This is primarily due to an
 568 increase in resolution, and not the reduced physics times-step; the *ne30pg3** run only marginally
 569 increases the extreme precipitation rates compared with *ne30pg3* (Figure 15).

570 The extreme precipitation rates in the *ARCTIC* run are closer to the ERA5 re-
 571 analysis than in *ne30pg3* (Figure 15). It's difficult to know the extent that the extreme
 572 precipitation rates in ERA5 are constrained by data assimilation, or whether these pre-
 573 cipitation rates are due to using a similar $\frac{1}{4}^{\circ}$ model as the *ARCTIC* grid. However, it
 574 is well documented that $\frac{1}{4}^{\circ}$ models are more skillful at simulating extreme events (Bacmeister
 575 et al., 2013; O'Brien et al., 2016), and so this is an additional benefit of the variable-resolution
 576 grids.

577 4 Conclusions

578 Six grids from different dynamical cores in CESM2.2 are evaluated in an AMIP-
 579 style configuration for their performance over the Arctic and in simulating the Green-
 580 land Ice Sheet (GrIS) surface mass balance (SMB). The $1-2^{\circ}$ finite-volume grids have
 581 enhanced resolution over polar regions due to the convergence of meridian lines, although
 582 a polar filter is employed to prevent atmospheric features from forming at this higher
 583 resolution. Spectral-element grids comparable to the resolution of the finite-volume grids
 584 have an isotropic grid structure, meaning the grid resolution is similar over the entire
 585 domain. Two variable-resolution grids were developed and introduced into CESM2.2 as

586 part of this work. They use the spectral-element dycore; the *ARCTIC* grid has $\frac{1}{4}^{\circ}$ refinement over the broader Arctic, whereas the *ARCTICGRIS* grid is identical except
 587 it has an $\frac{1}{8}^{\circ}$ patch of refinement over Greenland.
 588

589 In general, the finite-volume grids have colder summer temperatures over the Arctic
 590 compared with the spectral-element grids (incl. the variable-resolution grids). The
 591 cloud biases in all the uniform resolution grids, whether finite-volume or spectral-elements,
 592 are similar, in general being too cloudy over Arctic land masses. The variable-resolution
 593 grids largely improve the cloud biases. It should be emphasized that our analysis is spe-
 594 cific to the Arctic summer due to its relevance to melt rates over GrIS; improved clouds
 595 in the Arctic should not be taken to mean that lower latitude regions have an improved
 596 cloud field as well.

597 At the regional level, a halo of negative cloud bias is found around the oceanic perime-
 598 ter of Greenland in all $1-2^{\circ}$ grids, and is absent in the variable-resolution grids. This
 599 halo bias coincides with a positive cloud bias over the interior of the ice sheet. This pat-
 600 tern has been traced back to the inadequacy of the lower resolution grids to resolve the
 601 orographic precipitation process in Greenland. Synoptic systems moving into Greenland
 602 are not sufficiently lifted when encountering the steep ice margins due to overly smooth
 603 topography in the $1-2^{\circ}$ grids. As a result, moisture penetrates and dumps excess pre-
 604 cipitation into the interior of the GrIS, instead of being concentrated closer to the coastal
 605 margins as indicated by observations. This results in a positive precipitation and cloud
 606 bias in the ice sheet interior, and a halo of low cloud bias about the perimeter of Green-
 607 land. The agreement of different observational data products on this bias lends confi-
 608 dence in attributing the cause of the precipitation and cloud biases. The variable-resolution
 609 grids compare more favorably to the observations and indicate the orographic precip-
 610 itation process in Greenland is largely resolved.

611 The primary source and sink terms of the SMB equation are integrated over the
 612 GrIS, and evaluated in the six grids. The uniform $1 - 2^{\circ}$ grids all have large positive
 613 accumulation biases owing to their inability to resolve the orographic precipitation pro-
 614 cess. The uniform spectral-element grids have larger accumulation biases, suggesting that
 615 the finite-volume grids are more skillful at resolving the precipitation processes due to
 616 their finer grid spacing over Greenland, despite a polar filter. The variable resolution grids
 617 have the most accurate accumulation rates of all the grids.

618 The primary mass sink term of the GrIS, ice/snow melt, expresses similar biases
 619 as the accumulation rates. The uniform resolution spectral-element grids melt too much,
 620 while the finite-volume grids have reduced biases. It's more difficult to attribute these
 621 biases to grid resolution alone; the finite-volume grids have colder summers that is con-
 622 sistent with their lower melt bias. However, the *ARCTICGRIS* grid has the warmest
 623 summer temperatures of all grids, yet it has reduced melting compared to the uniform
 624 resolution spectral-element grids. This suggests that grid resolution is responsible for a
 625 large fraction of the melt biases. A mechanism is proposed; that coarse grids represent
 626 the ablation zones using mixed surface-type grid cells, and the ice-free patches of the cells
 627 may largely determine the volume mean state and lead to a warm bias over the ice cov-
 628 ered patches of the grid cell. This mechanism is supported by analysis of melt biases binned
 629 by grid cell ice fraction.

630 The *ARCTIC* grid provides substantial improvements to the simulated climate of
 631 the Arctic, such as precipitation extremes and the surface mass balance over Greenland,
 632 compared with the uniform $1^{\circ} - 2^{\circ}$ grids. The *ARCTICGRIS* grid has the most re-
 633 alistic cloud and precipitation fields, but suffers from excessive summer temperatures.
 634 The 1° finite-volume model provides a surprisingly realistic surface mass balance, likely
 635 due to the larger degrees of freedom used to represent the GrIS in latitude-longitude grids.
 636 In particular, the large number of grid cells representing the ablation zone leads to a re-

637 duction in mixed ice-covered/ice-free grid cells that seem to be so detrimental to the ab-
638 lation process in the other uniform resolution grids.

639 As modeling systems move away from latitude-longitude grids, and towards quasi-
640 uniform unstructured grids, it is worth taking stock as to whether this will adversely im-
641 pact the skill of the simulated climate in polar regions. In our case, we have found that
642 the 1° finite-volume model has clear advantages over the 1° spectral element model in
643 simulating the surface mass balance of the GrIS. While this finding is not sufficient to
644 slow-down the already ongoing transition towards unstructured grids in CESM, largely
645 driven by gains in computational efficiency, it has inspired us to develop alternative con-
646 figurations that recover the fidelity of polar climate in latitude-longitude grids. We have
647 shown in this study (and a prior companion study (van Kampenhout et al., 2018)), that
648 for CESM, the inclusion of Arctic refined meshes can substantially improve the simu-
649 lated mass balances of the GrIS, even compared with the finite-volume 1° grid. This should
650 provide the CESM modeling community with some comfort; the ongoing transition away
651 from latitude-longitude grids will not adversely impact CESM’s reputation as a state-
652 of-the-art tool for simulating and understanding polar processes.

653 We are actively working to develop a configuration of the *ARCTIC* mesh that is
654 fully-coupled with the CESM ocean model, and the Community Ice Sheet Model (CISM)
655 to provide multi-century projections of the state of the GrIS and its contribution to sea-
656 level rise. A fully-coupled pre-industrial control configuration has already been devel-
657 oped and vetted, and should be incorporated into CESM in the near-future. A visual-
658 ization of the *ARCTICGRIS* has been developed and made available on youtube¹ in or-
659 der to advertise some of the stunning capabilities of the refined mesh approach. A snap-
660 shot of this visualization is provided in Figure 16, illustrating mesoscale katabatic winds
661 descending down the southeastern slopes of GrIS. We are optimistic about the polar sci-
662 ence opportunities provided by these new Arctic mesh configurations, and our open to
663 collaborating with the CESM community to assist in anyway we can.

664 Acknowledgments

665 This material is based upon work supported by the National Center for Atmospheric Re-
666 search (NCAR), which is a major facility sponsored by the NSF under Cooperative Agree-
667 ment 1852977. Computing and data storage resources, including the Cheyenne super-
668 computer (doi:10.5065/D6RX99HX), were provided by the Computational and Informa-
669 tion Systems Laboratory (CISL) at NCAR. A. Herrington is especially grateful to W.
670 Lipscomb (NCAR) for providing crucial feedback in his ASP postdoc application, that
671 ultimately funded this study. A. Herrington also thanks Matt Rehme (NCAR/CISL) for
672 his role in generating the *ARCTICGRIS* visualization available on youtube (https://www.youtube.com/watch?v=YwHgqDu75s8&t=4s&ab_channel=NCARVisLab).

673 The data presented in this manuscript is available at <https://github.com/adamrher/2020-arcticgrids>.

676 References

- 677 Bacmeister, J. T., Wehner, M. F., Neale, R. B., Gettelman, A., Hannay, C., Lau-
678 ritten, P. H., ... Truesdale, J. E. (2013). Exploratory high-resolution climate
679 simulations using the community atmosphere model (cam). *J. Climate*, 27(9),
680 3073–3099. doi: 10.1175/JCLI-D-13-00387.1
681 Beljaars, A., Brown, A., & Wood, N. (2004). A new parametrization of turbulent
682 orographic form drag. *Quart. J. Roy. Meteor. Soc.*, 130(599), 1327–1347. doi:
683 10.1256/qj.03.73

¹ https://www.youtube.com/watch?v=YwHgqDu75s8&t=4s&ab_channel=NCARVisLab

- 684 Bogenschutz, P. A., Gettelman, A., Morrison, H., Larson, V. E., Craig, C., & Schaanen,
 685 D. P. (2013). Higher-order turbulence closure and its impact on climate
 686 simulations in the community atmosphere model. *Journal of Climate*, 26(23),
 687 9655–9676.
- 688 Braithwaite, R. J. (1984). Calculation of degree-days for glacier-climate research.
 689 *Zeitschrift für Gletscherkunde und Glazialgeologie*, 20(1984), 1–8.
- 690 Bromwich, D. H., Cassano, J. J., Klein, T., Heinemann, G., Hines, K. M., Steffen,
 691 K., & Box, J. E. (2001). Mesoscale modeling of katabatic winds over greenland
 692 with the polar mm5. *Monthly Weather Review*, 129(9), 2290–2309.
- 693 Calov, R., & Greve, R. (2005). A semi-analytical solution for the positive degree-day
 694 model with stochastic temperature variations. *Journal of Glaciology*, 51(172),
 695 173–175.
- 696 Canuto, C., Hussaini, M. Y., Quarteroni, A., & Zang, T. (2007). *Spectral methods:
 697 Evolution to complex geometries and applications to fluid dynamics* (1st ed.).
 698 Springer.
- 699 Chepfer, H., Bony, S., Winker, D., Cesana, G., Dufresne, J., Minnis, P., ... Zeng, S.
 700 (2010). The gcm-oriented calipso cloud product (calipso-goccp). *Journal of
 701 Geophysical Research: Atmospheres*, 115(D4).
- 702 Collins, W. D., Rasch, P. J., Boville, B. A., Hack, J. J., McCaa, J. R., Williamson,
 703 D. L., ... Zhang, M. (2006). The formulation and atmospheric simulation
 704 of the community atmosphere model version 3 (cam3). *Journal of Climate*,
 705 19(11), 2144–2161.
- 706 Copernicus, C. (2019). Era5 monthly averaged data on pressure levels from
 707 1979 to present. URL: <https://cds.climate.copernicus.eu>. doi: 10.24381/
 708 cds.6860a573
- 709 Craig, C., Bacmeister, J., Callaghan, P., Eaton, B., Gettelman, A., Goldhaber, S. N.,
 710 ... Vitt, F. M. (2021). *Cam6.3 user's guide* (Tech. Rep.). NCAR/TN-
 711 571+EDD. doi: 10.5065/Z953-ZC95
- 712 Danabasoglu, G., Lamarque, J.-F., Bacmeister, J., Bailey, D., DuVivier, A., Ed-
 713 wards, J., ... others (2020). The community earth system model ver-
 714 sion 2 (cesm2). *Journal of Advances in Modeling Earth Systems*, 12(2),
 715 e2019MS001916.
- 716 Danielson, J., & Gesch, D. (2011). *Global multi-resolution terrain elevation data
 717 2010 (GMTED2010)* (Open-File Report 2011-1073). U.S. Geological Survey.
 718 (<http://pubs.usgs.gov/of/2011/1073/pdf/of2011-1073.pdf>)
- 719 Dennis, J. M., Edwards, J., Evans, K. J., Guba, O., Lauritzen, P. H., Mirin, A. A.,
 720 ... Worley, P. H. (2012). CAM-SE: A scalable spectral element dynamical
 721 core for the Community Atmosphere Model. *Int. J. High. Perform. C.*, 26(1),
 722 74–89. Retrieved from <http://hpc.sagepub.com/content/26/1/74.abstract>
 723 doi: 10.1177/1094342011428142
- 724 Evans, K. J., Kennedy, J. H., Lu, D., Forrester, M. M., Price, S., Fyke, J., ... oth-
 725 ers (2019). Livykit 2.1: automated and extensible ice sheet model validation.
 726 *Geoscientific Model Development*, 12(3), 1067–1086.
- 727 Gettelman, A., Morrison, H., Santos, S., Bogenschutz, P., & Caldwell, P. (2015).
 728 Advanced two-moment bulk microphysics for global models. part ii: Global
 729 model solutions and aerosol–cloud interactions. *Journal of Climate*, 28(3),
 730 1288–1307.
- 731 Golaz, J.-C., Larson, V. E., & Cotton, W. R. (2002). A pdf-based model for bound-
 732 ary layer clouds. part i: Method and model description. *Journal of the Atmo-
 733 spheric Sciences*, 59(24), 3540–3551. doi: 10.1175/1520-0469(2002)059<3540:
 734 apbmfb>2.0.co;2
- 735 Guba, O., Taylor, M. A., Ullrich, P. A., Overfelt, J. R., & Levy, M. N. (2014). The
 736 spectral element method (sem) on variable-resolution grids: evaluating grid
 737 sensitivity and resolution-aware numerical viscosity. *Geosci. Model Dev.*, 7(6),
 738 2803–2816. doi: 10.5194/gmd-7-2803-2014

- 739 Guo, Z., Wang, M., Qian, Y., Larson, V. E., Ghan, S., Ovchinnikov, M., ... Zhou,
 740 T. (2015). Parametric behaviors of clubb in simulations of low clouds in the c
 741 ommunity atmosphere model (cam). *Journal of Advances in Modeling Earth*
 742 *Systems*, 7(3), 1005–1025.
- 743 Hansen, N., Simonsen, S. B., Boberg, F., Kittel, C., Orr, A., Souverijns, N., ... Mot-
 744 tram, R. (2022). Brief communication: Impact of common ice mask in surface
 745 mass balance estimates over the antarctic ice sheet. *The Cryosphere*, 16(2),
 746 711–718.
- 747 Herrington, A., Lauritzen, P., Taylor, M. A., Goldhaber, S., Eaton, B. E., Bacmeis-
 748 ter, J., ... Ullrich, P. (2018). Physics-dynamics coupling with element-based
 749 high-order galerkin methods: quasi equal-area physics grid. *Mon. Wea. Rev.*,
 750 47, 69–84. doi: 10.1175/MWR-D-18-0136.1
- 751 Herrington, A., & Reed, K. (2018). An idealized test of the response of the commu-
 752 nity atmosphere model to near-grid-scale forcing across hydrostatic resolutions.
 753 *J. Adv. Model. Earth Syst.*, 10(2), 560–575.
- 754 Herrington, A. R., Lauritzen, P. H., Reed, K. A., Goldhaber, S., & Eaton, B. E.
 755 (2019). Exploring a lower resolution physics grid in cam-se-cslam. *Journal of*
 756 *Advances in Modeling Earth Systems*, 11.
- 757 Herrington, A. R., & Reed, K. A. (2020). On resolution sensitivity in the commu-
 758 nity atmosphere model. *Quarterly Journal of the Royal Meteorological Society*,
 759 146(733), 3789–3807.
- 760 Hurrell, J. W., Hack, J. J., Shea, D., Caron, J. M., & Rosinski, J. (2008). A new
 761 sea surface temperature and sea ice boundary dataset for the community at-
 762 mosphere model. *Journal of Climate*, 21(19), 5145–5153.
- 763 Jablonowski, C., & Williamson, D. L. (2006). A baroclinic instability test case for
 764 atmospheric model dynamical cores. *Q. J. R. Meteorol. Soc.*, 132, 2943–2975.
- 765 Jablonowski, C., & Williamson, D. L. (2011). The pros and cons of diffusion, fil-
 766 ters and fixers in atmospheric general circulation models., in: P.H. Lauritzen,
 767 R.D. Nair, C. Jablonowski, M. Taylor (Eds.), Numerical techniques for global
 768 atmospheric models. *Lecture Notes in Computational Science and Engineering*,
 769 Springer, 80.
- 770 Lauritzen, P. H., Bacmeister, J. T., Callaghan, P. F., & Taylor, M. A. (2015). Ncar
 771 global model topography generation software for unstructured grids. *Geosci-
 772 entific Model Development Discussions*, 8(6), 4623–4651. doi: 10.5194/gmdd-8
 773 -4623-2015
- 774 Lauritzen, P. H., Mirin, A., Truesdale, J., Raeder, K., Anderson, J., Bacmeister, J.,
 775 & Neale, R. B. (2011). Implementation of new diffusion/filtering operators
 776 in the CAM-FV dynamical core. *Int. J. High Perform. Comput. Appl.*. doi:
 777 10.1177/1094342011410088
- 778 Lauritzen, P. H., Nair, R., Herrington, A., Callaghan, P., Goldhaber, S., Dennis, J.,
 779 ... Dubos, T. (2018). NCAR CESM2.0 release of CAM-SE: A reformulation
 780 of the spectral-element dynamical core in dry-mass vertical coordinates with
 781 comprehensive treatment of condensates and energy. *J. Adv. Model. Earth*
 782 *Syst.*. doi: 10.1029/2017MS001257
- 783 Lauritzen, P. H., Taylor, M. A., Overfelt, J., Ullrich, P. A., Nair, R. D., Goldhaber,
 784 S., & Kelly, R. (2017). CAM-SE-CSLAM: Consistent coupling of a conser-
 785 vative semi-lagrangian finite-volume method with spectral element dynamics.
 786 *Mon. Wea. Rev.*, 145(3), 833–855. doi: 10.1175/MWR-D-16-0258.1
- 787 Lawrence, D. M., Fisher, R. A., Koven, C. D., Oleson, K. W., Swenson, S. C., Bo-
 788 nan, G., ... others (2019). The community land model version 5: Description
 789 of new features, benchmarking, and impact of forcing uncertainty. *Journal of*
 790 *Advances in Modeling Earth Systems*, 11(12), 4245–4287.
- 791 Lin, S.-J. (2004). A 'vertically Lagrangian' finite-volume dynamical core for global
 792 models. *Mon. Wea. Rev.*, 132, 2293–2307.
- 793 Lin, S.-J., & Rood, R. B. (1997). An explicit flux-form semi-Lagrangian shallow-

- water model on the sphere. *Q.J.R.Meteorol.Soc.*, 123, 2477-2498.
- Lipscomb, W. H., Fyke, J. G., Vizcaíno, M., Sacks, W. J., Wolfe, J., Vertenstein, M., ... Lawrence, D. M. (2013). Implementation and initial evaluation of the glimmer community ice sheet model in the community earth system model. *Journal of Climate*, 26(19), 7352–7371.
- Loeb, N. G., Doelling, D. R., Wang, H., Su, W., Nguyen, C., Corbett, J. G., ... Kato, S. (2018). Clouds and the earth's radiant energy system (ceres) energy balanced and filled (ebaf) top-of-atmosphere (toa) edition-4.0 data product. *Journal of Climate*, 31(2), 895–918.
- Lofverstrom, M., Fyke, J. G., Thayer-Calder, K., Muntjewerf, L., Vizcaino, M., Sacks, W. J., ... Bradley, S. L. (2020). An efficient ice sheet/earth system model spin-up procedure for cesm2-cism2: Description, evaluation, and broader applicability. *Journal of Advances in Modeling Earth Systems*, 12(8), e2019MS001984.
- Neale, R. B., Richter, J. H., & Jochum, M. (2008). The impact of convection on ENSO: From a delayed oscillator to a series of events. *J. Climate*, 21, 5904–5924.
- Noël, B., Van De Berg, W., Van Meijgaard, E., Kuipers Munneke, P., Van De Wal, R., & Van Den Broeke, M. (2015). Evaluation of the updated regional climate model racmo2. 3: summer snowfall impact on the greenland ice sheet. *The Cryosphere*, 9(5), 1831–1844.
- Noël, B., van de Berg, W. J., Lhermitte, S., & van den Broeke, M. R. (2019). Rapid ablation zone expansion amplifies north greenland mass loss. *Science advances*, 5(9), eaaw0123.
- O'Brien, T. A., Collins, W. D., Kashinath, K., Rübel, O., Byna, S., Gu, J., ... Ullrich, P. A. (2016). Resolution dependence of precipitation statistical fidelity in hindcast simulations. *J. Adv. Model. Earth Syst.*, 8(2), 976–990. Retrieved from <http://dx.doi.org/10.1002/2016ms000671> doi: 10.1002/2016ms000671
- Ohmura, A. (2001). Physical basis for the temperature-based melt-index method. *Journal of applied Meteorology*, 40(4), 753–761.
- Pollard, D. (2010). A retrospective look at coupled ice sheet–climate modeling. *Climatic Change*, 100(1), 173–194.
- Pope, V., & Stratton, R. (2002). The processes governing horizontal resolution sensitivity in a climate model. *Climate Dynamics*, 19(3-4), 211–236.
- Putman, W. M., & Lin, S.-J. (2007). Finite-volume transport on various cubed-sphere grids. *J. Comput. Phys.*, 227(1), 55–78.
- Reeh, N. (1991). Parameterization of melt rate and surface temperature in the greenland ice sheet. *Polarforschung*, 59(3), 113–128.
- Richter, J. H., Sassi, F., & Garcia, R. R. (2010). Toward a physically based gravity wave source parameterization in a general circulation model. *J. Atmos. Sci.*, 67, 136–156. doi: dx.doi.org/10.1175/2009JAS3112.1
- Rignot, E., & Mouginot, J. (2012). Ice flow in greenland for the international polar year 2008–2009. *Geophysical Research Letters*, 39(11).
- Roeckner, E., Brokopf, R., Esch, M., Giorgetta, M., Hagemann, S., Kornblueh, L., ... Schulzweida, U. (2006). Sensitivity of simulated climate to horizontal and vertical resolution in the echam5 atmosphere model. *Journal of Climate*, 19(16), 3771–3791.
- Sellevold, R., Van Kampenhout, L., Lenaerts, J., Noël, B., Lipscomb, W. H., & Vizcaino, M. (2019). Surface mass balance downscaling through elevation classes in an earth system model: Application to the greenland ice sheet. *The Cryosphere*, 13(12), 3193–3208.
- Smirnova, J., & Golubkin, P. (2017). Comparing polar lows in atmospheric reanalyses: Arctic system reanalysis versus era-interim. *Monthly Weather Review*, 145(6), 2375–2383.

- 849 Stocker, T. (2014). *Climate change 2013: the physical science basis: Working group*
850 *i contribution to the fifth assessment report of the intergovernmental panel on*
851 *climate change*. Cambridge university press.
- 852 Suarez, M. J., & Takacs, L. L. (1995). Volume 5 documentation of the aries/geos dy-
853 namical core: Version 2.
- 854 Taylor, M. A., & Fournier, A. (2010). A compatible and conservative spectral el-
855 ement method on unstructured grids. *J. Comput. Phys.*, 229(17), 5879 - 5895.
856 doi: 10.1016/j.jcp.2010.04.008
- 857 Taylor, M. A., Tribbia, J., & Iskandarani, M. (1997). The spectral element method
858 for the shallow water equations on the sphere. *J. Comput. Phys.*, 130, 92-108.
- 859 Team, E. J. S., Balaji, V., Boville, B., Collins, N., Craig, T., Cruz, C., ... others
860 (2021). *Esmf user guide* (Tech. Rep.).
- 861 Ullrich, P. A., & Taylor, M. A. (2015). Arbitrary-order conservative and consis-
862 tent remapping and a theory of linear maps: Part i. *Monthly Weather Review*,
863 143(6), 2419–2440.
- 864 Ullrich, P. A., Zarzycki, C. M., McClenny, E. E., Pinheiro, M. C., Stansfield, A. M.,
865 & Reed, K. A. (2021). Tempestextremes v2. 1: a community framework for
866 feature detection, tracking and analysis in large datasets. *Geoscientific Model
867 Development Discussions*, 1–37.
- 868 van Kampenhout, L., Lenaerts, J. T., Lipscomb, W. H., Lhermitte, S., Noël, B.,
869 Vizcaíno, M., ... van den Broeke, M. R. (2020). Present-day greenland ice
870 sheet climate and surface mass balance in cesm2. *Journal of Geophysical
871 Research: Earth Surface*, 125(2).
- 872 van Kampenhout, L., Rhoades, A. M., Herrington, A. R., Zarzycki, C. M., Lenaerts,
873 J. T. M., Sacks, W. J., & van den Broeke, M. R. (2018). Regional grid refine-
874 ment in an earth system model: Impacts on the simulated greenland surface
875 mass balance. *The Cryosphere Discuss..* doi: 10.5194/tc-2018-257
- 876 Williamson, D. (2007). The evolution of dynamical cores for global atmospheric
877 models. *J. Meteor. Soc. Japan*, 85, 241-269.
- 878 Williamson, D. L. (2008). Convergence of aqua-planet simulations with increas-
879 ing resolution in the community atmospheric model, version 3. *Tellus A*, 60(5),
880 848–862. doi: 10.1111/j.1600-0870.2008.00339.x
- 881 Zhang, G., & McFarlane, N. (1995). Sensitivity of climate simulations to the pa-
882 rameterization of cumulus convection in the canadian climate centre general
883 circulation model. *Atmosphere-ocean*, 33(3), 407-446.

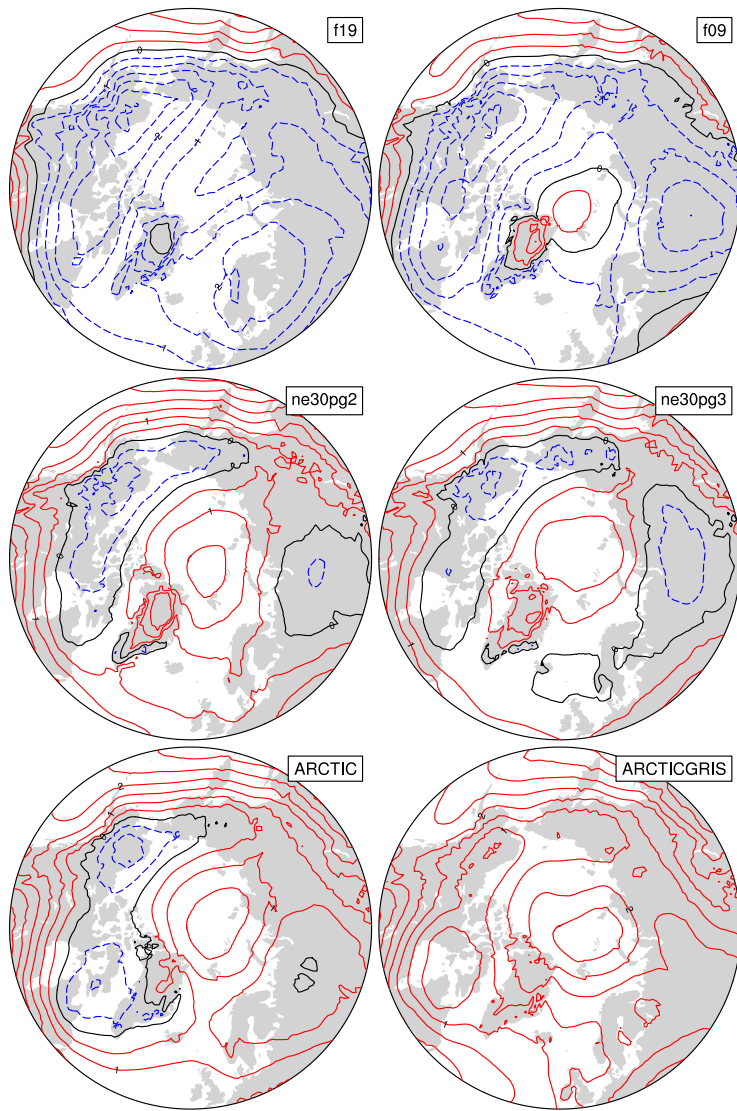


Figure 6. 1979-1998 lower troposphere, northern hemisphere summer virtual temperature biases, computed as the difference from ERA5. Lower troposphere layer mean virtual temperature is derived from the 1000 hPa - 500h Pa geopotential thickness, using the hypsometric equation. Differences are computed after mapping the ERA5 data to the finite-volume grids since the geopotential field is only available on the output tapes in the spectral-element runs that have been interpolated to the *f09* grid, inline.

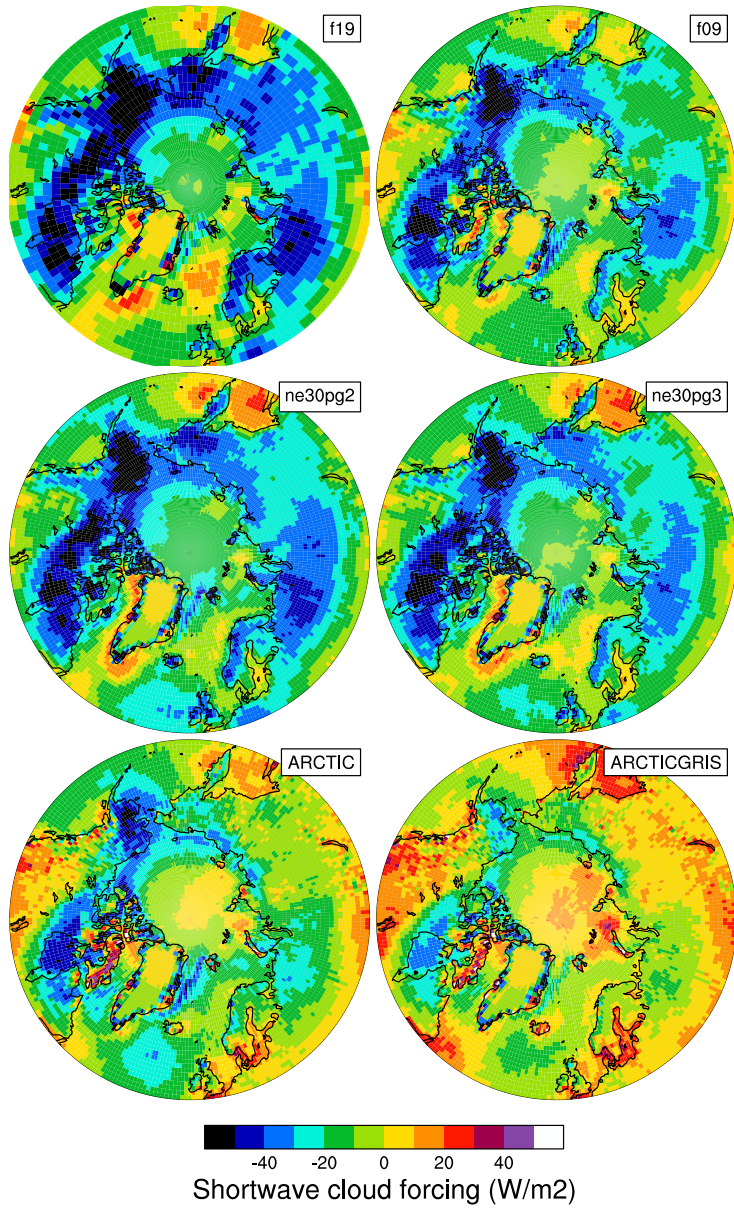


Figure 7. 1979-1998 northern hemisphere summer shortwave cloud forcing bias, relative to the CERES-EBAF gridded dataset. Differences are computed after mapping all model output to the 1° CERES-EBAF grid.

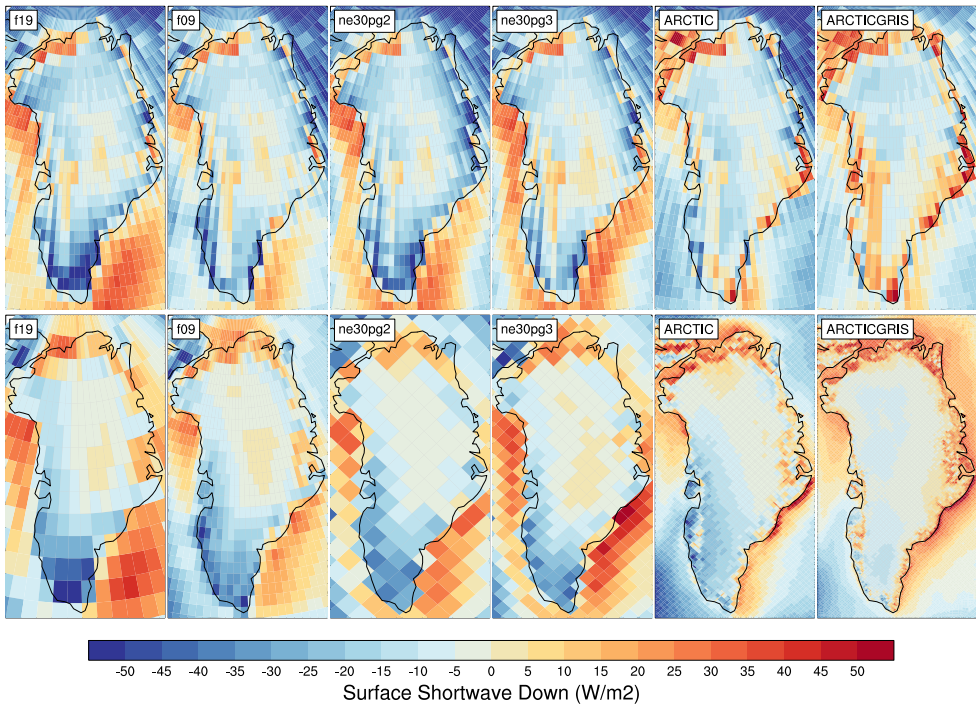


Figure 8. 1979-1998 northern hemisphere summer, incident shortwave radiation bias, computed as the difference (top) from CERES-EBAF, and (bottom) RACMO2.3p2 dataset. The differences in the top panel are found by mapping the model output to the 1° CERES-EBAF grid, and differences on the bottom panel are computed after mapping the RACMO2.3p2 dataset to the individual model grids. Note that the averaging period for the CERES-EBAF panels, 2003-2020, is different from the averaging period for the model results.

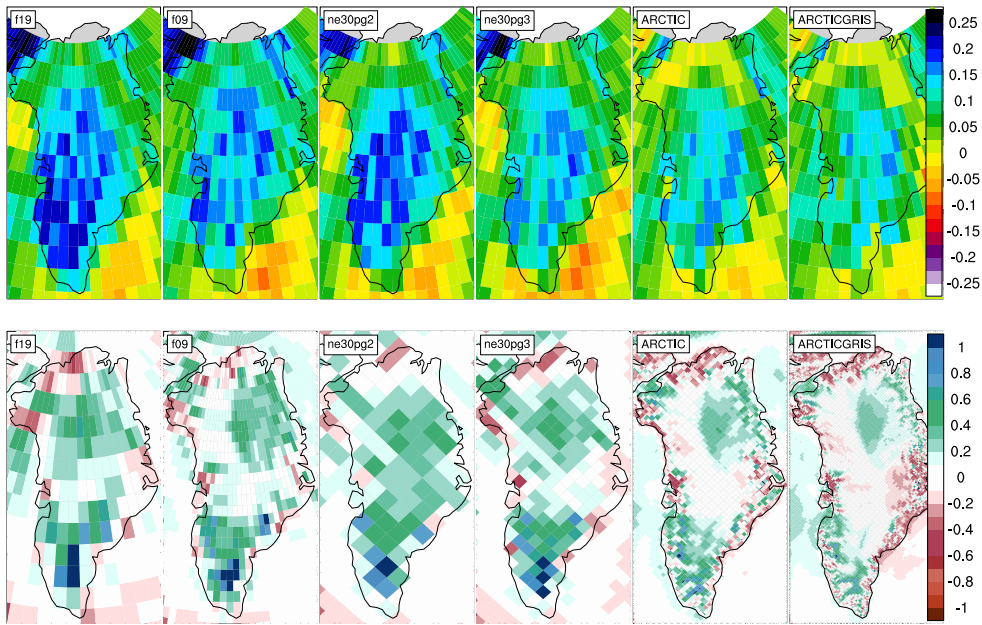


Figure 9. 1979-1998 northern hemisphere summer (top) total cloud fraction bias, relative to the CALIPSO-GOCCP dataset, and (bottom) precipitation rate bias, relative to the RACMO2.3p2 dataset. The CALIPSO-GOCCP differences are computed after mapping all model output to the 1° grid, whereas the RACMO differences are computed after mapping the RACMO dataset to the individual model grids. Note that the averaging period for the CALIPSO-GOCCP panels, 2006-2017, is different than the model averaging period. **ARH** - still trying to fix the layout of this figure so the label bars aren't on top of the panels.

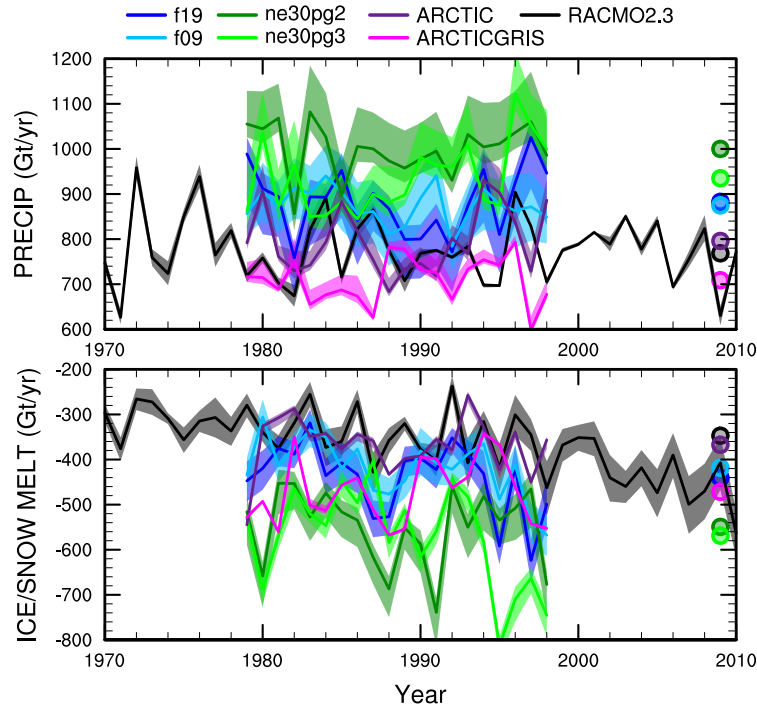


Figure 10. Time-series of annual (solid+liquid) precipitation (top) and annual runoff (bottom) integrated over the Greenland Ice Sheet for all six simulations and compared to the RACMO datasets. The time-series were generated using the common ice mask approach, which results in up to 4 ensembles, with the mean value given by the solid line and shading spanning the extent of the ensemble members.

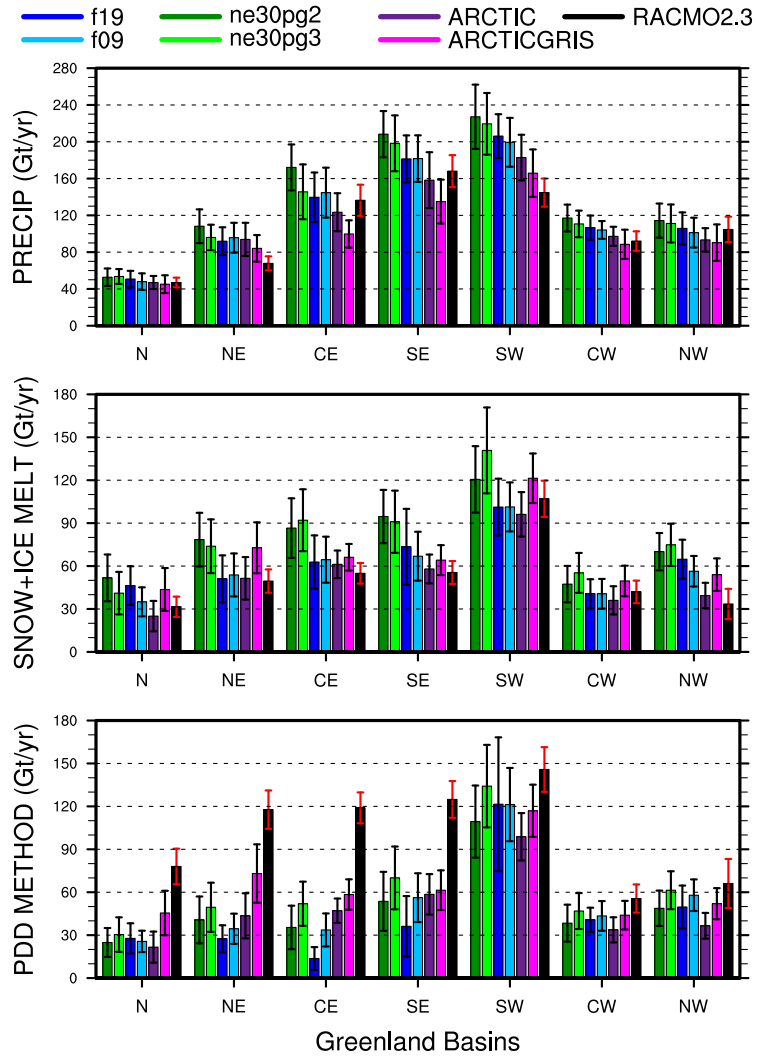


Figure 11. 1979-1998 basin integrated components of the SMB; (top) precipitation, (middle) ice/snow melt and (bottom) ice/snow melt estimated from the PDD method. Whiskers span the max/min of the 4 ensemble members generated from the common ice mask approach. Basin definitions are after Rignot and Mouginot (2012), and are found on the common ice masks using a nearest neighbor approach, and shown in Figure 12.

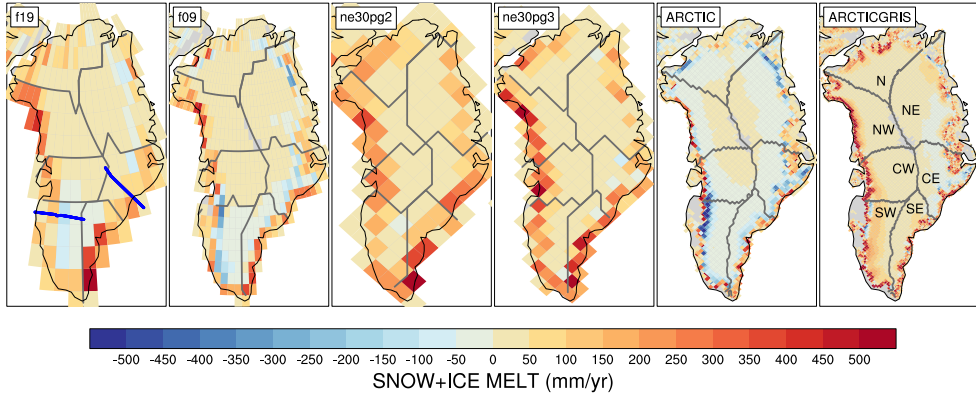


Figure 12. 1979–1998 ice/snow melt biases (in mm/yr) relative to RACMO2.3p2, evaluated on the native model grids. The Rignot and Mouginot (2012) basin boundaries are shown in grey for each model grid. Note that Figure 11 uses the basin boundaries for the two common ice masks, shown in the *f19* and *ne30pg2* panels, in computing the basin-scale integrals. Blue lines in the *f19* panel show the location of the two transects plotted in Figure 13.

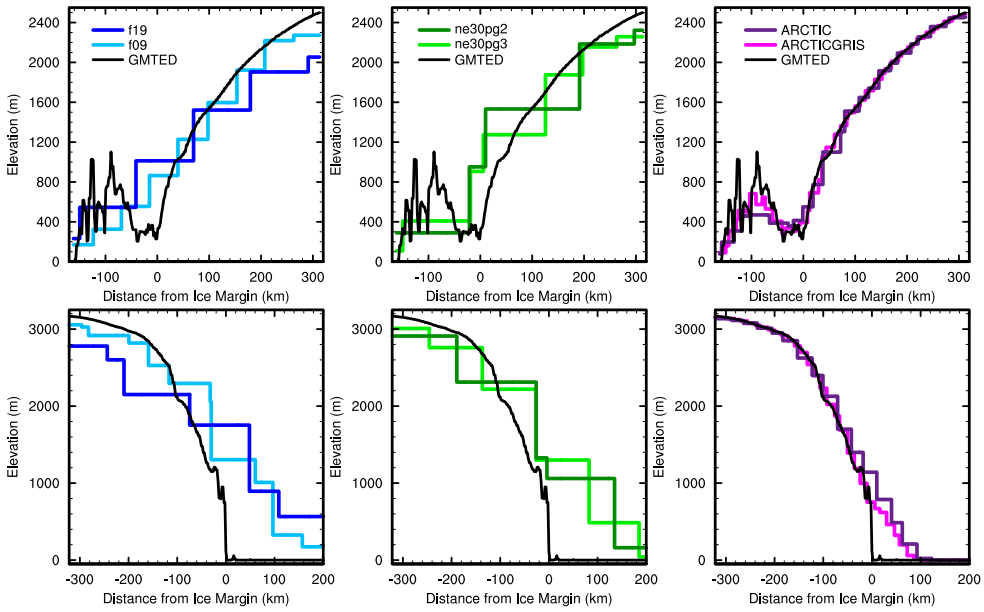


Figure 13. Model surface elevation along the (top) k-transect, and (bottom) a transect spanning the central dome, down to the Kangerlussuaq glacier in southeast Greenland, for all model grids. The reference surface (GMTED) is a 1 km surface elevation dataset used for generating the CAM topography boundary conditions.

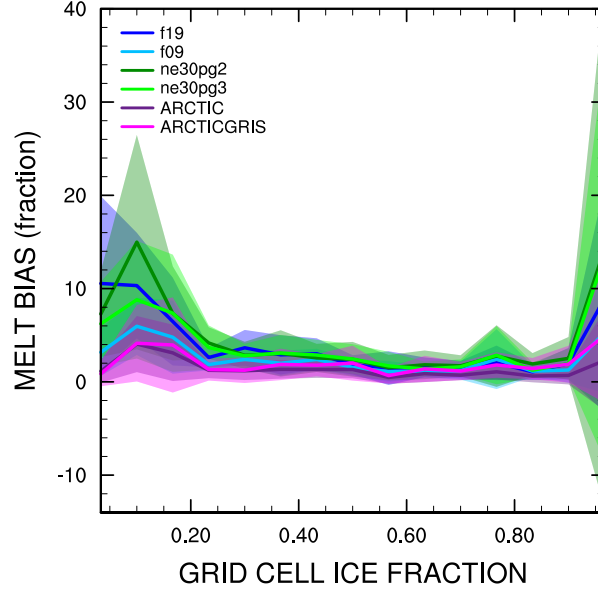


Figure 14. Fractional melt bias over the GrIS, computed relative to the RACMO datasets using the common ice mask approach, and conditionally sampled by grid cell ice fraction provided by the common ice masks. Solid lines are the mean of the distribution with \pm one standard deviation expressed by shading.

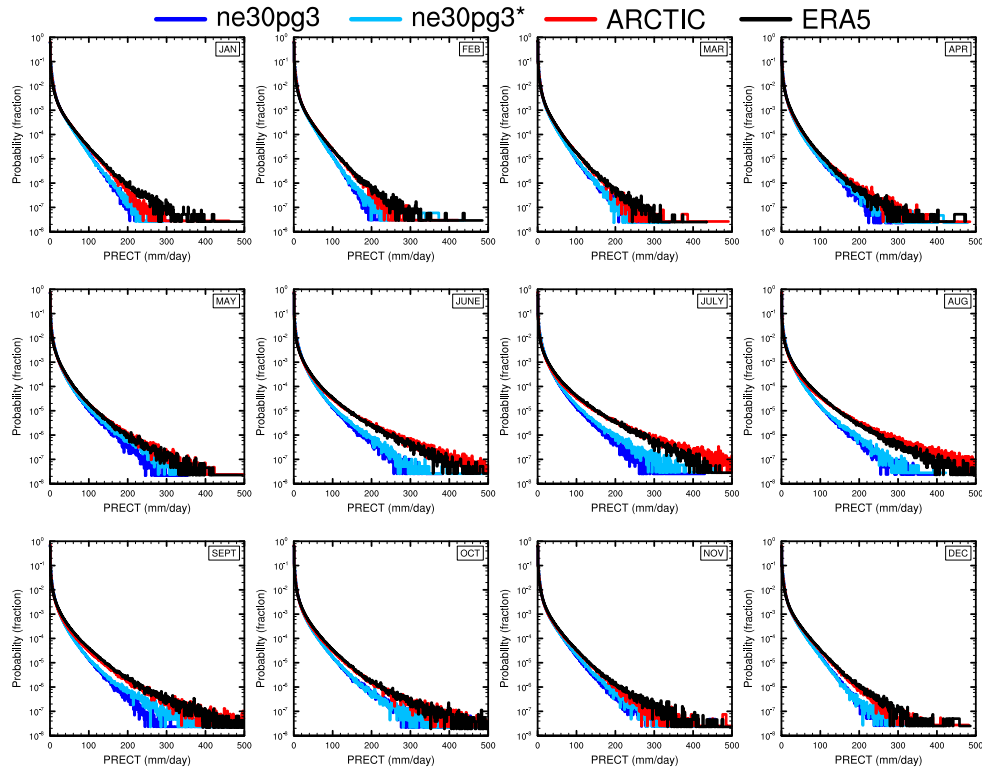


Figure 15. PDFs of the total precipitation rate associated with tracked storms, by month, in the *ne30pg3*, *ne30pg3** and *ARCTIC* runs, and compared with the ERA5 dataset.

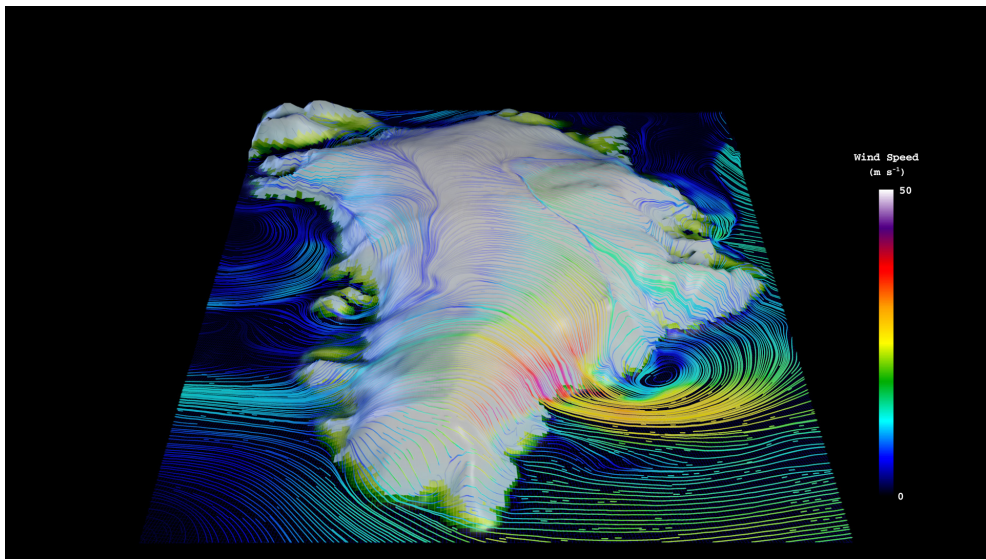


Figure 16. Snapshot of the lowest model level streamlines from the *ARCTICGRIS* visualization, with color shading denoting the wind magnitude.